

Metasurface-Based Fiber-to-Chip Multiplexing Coupler


Rui Chen, Yu-ke Chang, Ze-peng Zhuang, Yan Liu, Wen-jie Chen,* and Jian-wen Dong*

Here, a metasurface-based fiber-to-chip multiplexing coupler is presented that can realize flexible mode conversion and multiplexing coupling between few-mode fibers and on-chip single-mode waveguides. The proposed approach makes use of the symmetrical characteristics of fiber eigenmodes and high freedom of light phase manipulation to obtain the functional phase distribution of metasurfaces. The use of cylindrical nanopillar as metasurface nanostructures ensures its polarization independent optical response. Several fiber-to-chip multiplexing couplers are demonstrated by using the angular spectrum methods and the finite-difference time-domain (FDTD) simulations. It is found that the two or three modes can be flexibly demultiplexed and then be coupled into the corresponding on-chip waveguides with low crosstalk. Further, two possible fabrication schemes for multiplexing couplers are proposed and then the related fabrication tolerances and misalignment effects are evaluated and discussed. Compared with traditional on-chip couplers, metasurface-based couplers have advantages of ultracompact footprint and low crosstalk. Such study explores the application of metasurfaces in multiplexing coupling between few-mode fiber and on-chip single-mode waveguides, which is expected to break through the bottleneck of current mode-division multiplexing technologies in optical interconnection and meet the ever-increasing demand for large data throughput of the photonic integrated chips.

1. Introduction

The efficient coupling of light from optical fibers into integrated waveguides is of major importance in photonic integrated devices such as photodiodes, semiconductor optical amplifier and so on.^[1–4] As is known to all, the feature size of integrated waveguide structures can be as tiny as tens of nanometers due to the increasing integrated density while typical diameter of a single-mode-fiber (SMF) is around 125 μm with a core diameter near 10 μm .^[2] Such huge geometry difference between fiber and the on-chip waveguide leads to large mismatch of the mode field. To this end, two types of couplers, grating couplers^[5–8] and edge couplers,^[9–13] have been developed to mitigate mismatch of mode fields and reduce the coupling loss.

R. Chen, Y.-k. Chang, Z.-p. Zhuang, Y. Liu, W.-j. Chen, J.-w. Dong
School of Physics & State Key Laboratory of Optoelectronics Materials
and Technologies
Sun Yat-sen University
Guangzhou 510275, P. R. China
E-mail: chenwenj5@mail.sysu.edu.cn; dongjwen@mail.sysu.edu.cn

 The ORCID identification number(s) for the author(s) of this article can be found under <https://doi.org/10.1002/adom.202202317>.

DOI: 10.1002/adom.202202317

Among them, the grating coupler uses the principle of grating diffraction to couple light into the optical fiber vertically, which results in its inherent shortcomings, namely the limited bandwidth and lower coupling efficiency. Compared to the grating couplers, edge couplers achieve adiabatic evolution of mode field and change the size of the spots by designing and optimizing complex waveguide structures at end-facet of the chip. The adiabatic evolution can enable guide mode to propagate and convert into other modes with little reflection or scattering losses. Although high coupling efficiencies up to 93% (−0.32 dB) have been achieved,^[14] most of these schemes are based on the fundamental mode coupling of SMFs with on-chip single-mode waveguides.

With the continued exponential growth of data traffic, the transmission capacity of conventional SMF has already approached the Shannon's limit. To solve this problem, mode-division multiplexing (MDM) technologies have been developed to enhance the capacity of optical fiber transmission since it could exploit the spatial dimension and multiplex parallel information

path into independent orthogonal spatial modes. As a result, it is imperative to address high-order modes coupling challenge. For example, a grating coupler between the LP₁₁ mode in the few-mode-fibers (FMF) and the first-order transverse electric (TE) mode in the waveguide of the silicon-on-insulator (SOI) chip has been investigated, which consists of a double-part grating structure that couples the two petals of the first-order mode and a Y-junction that is used for the petal combination.^[15] For the case of edge coupling, a spot size converter (SSC), composed of a double-tip inverse taper and a Y-junction structure, has been also reported to couple an SOI waveguide mode and the LP₁₁ mode of an FMF.^[16]

However, these structures are adopted for the first high-order fiber mode coupling only. In the on-chip MDM optical network, the simultaneous multimode coupling of FMFs and the on-chip waveguides is a still challenging task due to the large geometry and index mismatch between the FMF and waveguides. The two parallel inverse tapers are expanded to a triple-tip inverse taper for two-mode coupling.^[17,18] Besides, based on the phase matching condition, three-dimensional asymmetric waveguides structure^[19] and stacked polymer waveguide structure,^[20] are reported to serve as interface between FMF and the on-chip integrated waveguide. Nevertheless, these waveguide-based edge couplers should always be carefully designed and

optimized to meet the need of multimode coupling, which increases the complexity of fabrication. In addition, these structures may face the challenge of large footprints and limited operation bandwidth.

Recently, metasurfaces, a 2D metamaterial,^[21,22] has demonstrated strong potentials in various optical devices such as flat metalens,^[23–25] wave plates,^[26] vortex beam generators,^[27] and vector beam generators,^[28] due to its ultracompact footprint, versatile functionalities and capability of exploiting multiple degree of freedoms to manipulate the light at the subwavelength scale. In addition, the metasurface-based MDM technology has been also demonstrated in free space optical communication configurations. For example, the orthogonally polarized LP₀₁ modes are multiplexed into LP₁₁ and LP₁₂ high-order linear polarized modes^[29] or high-order vector modes.^[30] Consequently, metasurfaces combined with the optical fibers are expected to be a promising candidate for mode (de)multiplexing in FMF-MDM systems, which may replace conventional functional devices, simplify the complexity and ultimately contribute to miniaturization and integration of optical systems.

In this paper, we propose a metasurface-based multiplexing coupler, which not only acts as a fiber mode demultiplexer to demultiplex the fiber modes, for example, LP₀₁ and LP₁₁, into the different mode channels, but also acts as a fiber-to-chip mode converter and coupler, enabling mode conversion and mode coupling. The functional phase distribution of the metasurfaces is determined by focusing design and the region division scheme that is based on the symmetric characteristic of

fiber eigenmodes. To achieve polarization insensitiveness, the cylindrical pillars are adopted as the metasurface nanostructures, the optical response of which has the same phase shift for both polarizations. Dual-mode and triple-mode multiplexing couplings are designed and then validated by angular spectrum method and the finite-difference time-domain (FDTD) simulations. It is found that the crosstalk between the fiber modes is quite low. Therefore, we can integrate mode demultiplexing and mode coupling through a planar subwavelength structure only, which is beneficial to the integration and miniaturization of coupling systems.

The remainder of the paper is organized as follows. In Section 2, the schematic diagram of the metasurface-based fiber-to-chip multiplexing coupler is introduced. In Section 3, dual-mode and triple-mode multiplexing couplers are presented and some discussions of fabrication schemes are provided in details. Finally, conclusions are drawn in Section 4.

2. The Schematic Design of the Metasurface-Based Multiplexing Coupler

The schematic configuration of the metasurface-based multiplexing coupler is shown in **Figure 1**, which consists of a standard few-mode optical fiber, a SiO₂ spacer on which the metasurface nanostructures locate, SSC and silicon photonics wire waveguides. Without loss of generality, two fiber modes at working wavelength of $\lambda = 1550$ nm, LP₀₁ and LP₁₁, propagate

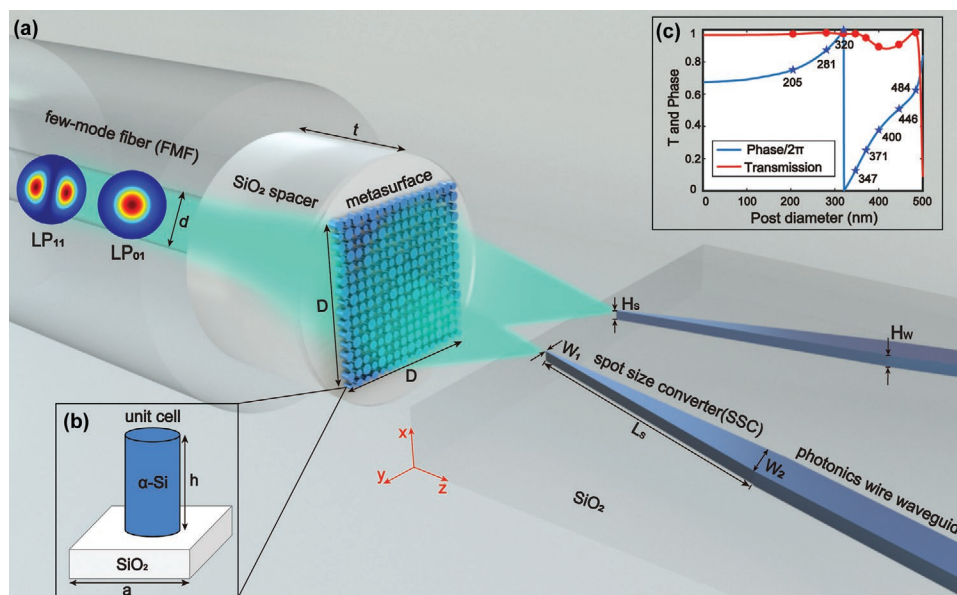


Figure 1. The schematic illustration of the metasurface-based multiplexing coupler. a) The configuration is composed of a few-mode optical fiber, a SiO₂ spacer attached with metasurface nanostructures, spot size converters, and silicon photonics wire waveguides. The thickness of the SiO₂ spacer is $t = 250$ μm . On the waveguide side, for each inverted taper structure of thickness $H_s = H_w = 220$ nm, serving as SSC, the transverse width is gradually changed from $W_2 = 500$ nm to $W_1 = 180$ nm. As an example, two fiber modes, LP₀₁ and LP₁₁, propagate through the SiO₂ spacer and are then modulated by a carefully designed metasurfaces to generate the reduced mode fields that could couple with the spot size converters at the different locations. The unit cell of the metasurface nanostructures is shown in (b). A silicon nanopillar of refractive index 3.48 and height $h = 750$ nm stands on the silicon dioxide substrate with refractive index of 1.444. The subwavelength lattice constant a is set to 600 nm. c) The transmission coefficient and phase of the unit cell as a function of the post diameter, which shows the full 2π phase coverage and the close-to-one transmission spectrum for a family of α -Si periodic gratings at $\lambda = 1550$ nm. The eighth-order α -Si circular nanopillars (red dots and blue stars) are chosen to provide the full 2π phase coverage, which is polarization insensitive for normal incidence due to the geometric symmetry.

through the SiO₂ spacer of thickness $t = 250 \mu\text{m}$ and are then modulated by metasurfaces to generate reduced mode fields. The core diameter of the dual-mode fiber d is $14 \mu\text{m}$, and the refractive indices of the core and cladding layers are 1.4485 and 1.444, respectively. On the waveguide side, for each inverted taper structure of thickness $H_s = H_w = 220 \text{ nm}$, serving as SSC, the transverse width is gradually changed from $W_2 = 500 \text{ nm}$ to $W_1 = 180 \text{ nm}$. As the transverse width of the taper decreases, the localization of the guided mode deteriorates, and the guided mode gradually diffuses into the lower refractive index cladding, resulting in the increase in the size of the mode field and the decline in the effective refractive index. This mode field could be matched with the reduced model field from metasurfaces. The effective refractive index of the fundamental LP₀₁ mode is 1.447 while the effective refractive index of the LP₁₁ mode 1.445.

Here, the metasurface not only acts as a fiber mode demultiplexer to demultiplex fiber modes into different mode channels, but also acts as a fiber-to-chip mode coupler, enabling dual-mode coupling. Such implementation of the two functions of mode demultiplexing and mode coupling through a planar sub-wavelength structure is beneficial to the integration and miniaturization of the photonics integrated system. The design of the metasurface-based coupler can be divided into threefold. First, each fiber mode has to be focused to the corresponding spatial location of the waveguides as shown in Figure 1, therefore the phase distribution of the metasurfaces should be given by

$$\phi(x, y; l) = -\frac{2\pi}{\lambda} \left(\sqrt{x^2 + (y+l)^2 + f^2} - |f| \right) \quad (1)$$

where the (x, y) denotes the Cartesian coordinate on the metasurfaces and f is the focal length of the designed metasurfaces. The location of the reduced mode fields can be determined by adjusting the value of l . It should be noted that more than one fiber modes propagate through the metasurfaces. Therefore, the idea of the second step is to raise the region division scheme of metasurfaces. More specifically, the metasurfaces are divided into regions according to the number and characteristics of fiber modes. Some of these regions constructively focus a fiber mode to the corresponding wire waveguide location to which the other fiber modes are destructively focused, and vice versa. Fortunately, the symmetric characteristics of the intensity and phase distribution of the fiber modes provide another guarantee. So far, the functional phase distribution of the metasurfaces is determined and then how to achieve such phase distribution using metasurface nanostructures is the work of the next step.

In the third step, to achieve polarization insensitive metasurfaces, a cylindrical nanopillar is chosen as the nanostructure. The schematic design of α -Si periodic grating and unit cell is illustrated in Figure 1b. The nanopillar is made of Silicon, whose refractive index is 3.48, and stands on the silicon dioxide substrate of refractive index 1.444. To achieve a full 2π coverage, we set the subwavelength lattice constant a to be 600 nm , which ensures only zero diffraction survive. In addition, the height h of nanopillar is set to 750 nm according to the simulations. Simulations of α -Si periodic gratings using rigorous coupled-wave analysis (RCWA)^[31] are presented to demonstrate the targeted transmission spectra and phase response in Figure 1c.

It is found that the proposed α -Si nanopillars with diameter ranging from 0 to near 500 nm can support high transmission (blue curve) and a full 2π phase coverage (red curve) at the operating wavelength of 1550 nm . Therefore, we choose the eighth-order α -Si circular nanopillars with diameters of 320, 347, 371, 400, 446, 484, 205, and 281 nm , respectively, to provide the full 2π phase coverage. The corresponding transmission coefficients are 0.974, 0.973, 0.949, 0.893, 0.907, 0.98, 0.972, and 0.98, respectively.

We take the two fiber modes for example, LP₀₁ and LP₁₁, to explicitly illustrate the process of the metasurfaces design. The amplitude and phase profile of two modes are shown in Figure 2a,b, respectively. The metasurfaces can be uniformly divided into three regions as shown in Figure 2c. For convenience, we use I to refer to the middle one, while II and II' for the left and right one, respectively. The phase distribution of region I , II , and II' are chosen as $\phi(x, y; l)$, $\phi(x, y; -l)$, and $\phi(x, y; -l) - \pi$ from Equation (1), respectively. For the LP₀₁ mode, a fundamental mode of Gaussian-like beam with a uniform phase distribution in Figure 2a, it can be focused by region I to a reduced focal spot a on the y axis due to the constructive interference. In the contrast, there is a destructive interference at the point a' of y axis when it passes the region II and II' . Consequently, the LP₀₁ mode could be well brought in the corresponding wire waveguide location, a , as shown in Figure 2d.

For the LP₁₁ mode in Figure 2b, its intensity distribution shows two symmetric maxima away from the optical axis in the direction of the polarization of the electric field. The phases of the two petals are 0 and π , respectively. These characteristics inspire us the idea of the region division scheme and the π phase difference setting of regions II and II' . When the LP₁₁ mode propagates through region I and then focus to the point a on y axis, the destructive interference occurs. When the LP₁₁ mode propagates through region II and II' and then focuses to the point a' on the y -axis, the constructive interference occurs. In a word, with the properly designed functional metasurfaces, the LP₀₁ and LP₁₁ mode can be focused on points a and a' in the form of central bright spots, respectively. It implies that mode-selective focusing and mode demultiplexing of modes can be realized simultaneously by the careful designed metasurfaces, which is based on its high freedom of the light manipulation and the symmetric characteristics of the fiber eigenmodes. In addition, our metasurfaces is independence of the polarization state of the incident light due to the circular symmetry of the selected nanostructures. When more than two fiber modes propagate in the optical path, the similar design can be used, the detail of the which can be found in the following Sections.

3. Results and Discussions

To validate the proposed metasurface-based fiber-to-chip multiplexing coupler, simulations regarding two or three fiber modes are provided in this Section. The parameters of the setup are the same as that in previous Section. Specifically, first, the phase profile of the metasurfaces is designed by the region division scheme taking full advantage of the symmetrical characteristic of fiber eigenmodes. Based on the ideal composite phase

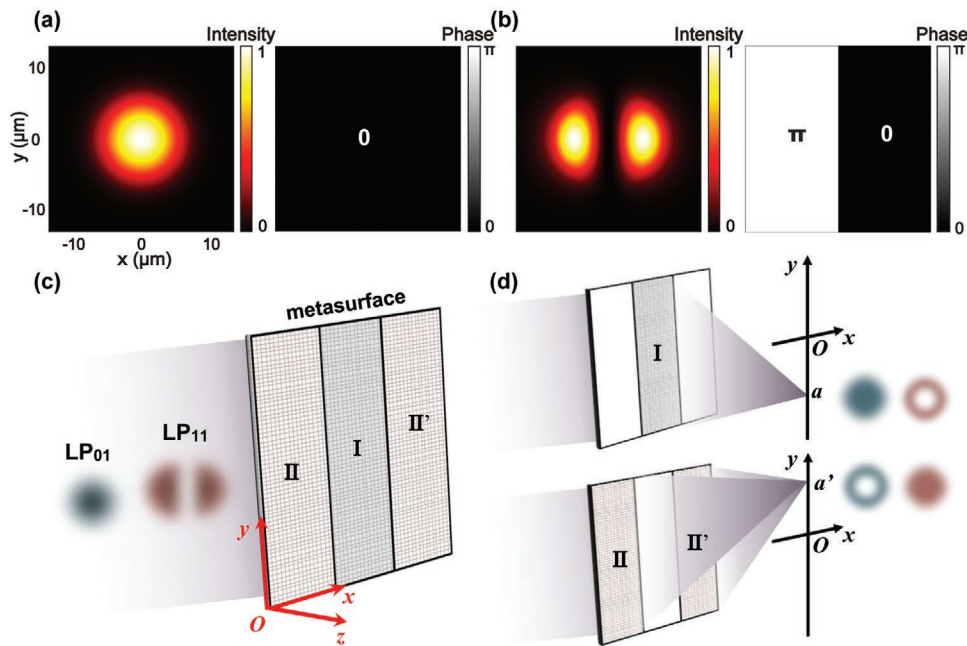


Figure 2. The schematic diagram of the metasurface design when two fiber nodes, LP₀₁ and LP₁₁, are considered as an example. a) The amplitude and phase profiles of the LP₀₁ mode and b) the amplitude and phase profiles of LP₁₁ mode. c) The region division scheme of metasurfaces for the two fiber modes, LP₀₁, and LP₁₁. d) The focusing profiles at the different location of a and a' .

profiles (focusing and focus shift in Figure 1), the angular spectrum method is employed to simulate light propagation and the intensity profiles for mode-selective focusing. To clearly show the function of the metasurfaces, the comparison of the mode field size of different modes before and after metasurface focusing are offered for the following dual-mode and triple-mode multiplexing couplers (Please see Figures S1–S4 in Section S1, Supporting Information). Furthermore, the ideal phase profile is implemented by the basis of eight types of polarization-insensitive nanopillars with different diameters. The full-wave analysis is performed by FDTD simulation.

To evaluate the performance on mode conversion and coupling, several evaluation parameters are provided here. The first one is coupling efficiency η , which can be expressed as the overlap between the fiber mode and the tapered waveguide mode

$$\eta = \frac{\left| \iint E_1 \cdot \text{conj}(E_2) dx dy \right|^2}{\int |E_1|^2 dx dy \int |E_2|^2 dx dy} \quad (2)$$

where E_1 and E_2 stand for the complex electric field amplitudes of the fiber mode and the mode at the chip facet, respectively, $\text{conj}(\cdot)$ denotes the conjugate of the complex electric field. The second one is crosstalk (CT), which is defined as unwanted transfer of signals between communication channels, as given by

$$CT_{ij} = 10 \log(P_j/P_i) \quad (3)$$

where P_j and P_i stand for unwanted noise signal and working signal in the i th-channel, respectively.

3.1. Dual-Mode Metasurface-Based Multiplexing Coupler

In Section 2, the ideal phase profile design for dual mode fiber demultiplexing has been provided. The metasurfaces can be uniformly divided into three regions with the phase profiles, $\phi(x, y; l)$, $\phi(x, y; -l)$, and $\phi(x, y; -l) - \pi$ from Equation (1), respectively. Based on the phase profile, the angular spectrum method is used for the light propagation simulation. When two fiber modes are imparted by the phase profile, two modes are manipulated to the customized mode fields. The light intensity on the y - z plane (the left column) for LP₀₁ or LP₁₁ incidence is plotted in Figure 3a,d, respectively. The simulated normalized intensity distribution at the corresponding focal plane (LP₀₁: $z = 30.82 \mu\text{m}$, LP₁₁: $z = 33.49 \mu\text{m}$) are also provided in the right column of Figure 3a,d. It is found that the LP₀₁ and LP₁₁ modes are demultiplexed into different spatial transmission channels, a and a' .

To demonstrate modes demultiplexing and coupling using metasurfaces, furthermore, the overall process of coupling fiber modes into tapered waveguides is simulated using FDTD. It is noted that the inverse taper waveguide in Figure 3b,e has a deflection angle that is determined by the orientation of the beam propagation focused by metasurfaces in Figure 3a,d, which is also applicable to the following dual-mode and triple-mode multiplexing couplers. After the transmission of the metasurface, the output of LP₀₁ mode is limited in the lower right wire waveguide (Figure 3c), while the transmission of LP₁₁ mode is localized in the upper right waveguide (Figure 3f). To clearly see the mode field in the wire waveguide, the evolution of mode field for LP₀₁ mode along the inverted taper structure is shown in Figure S5 (Supporting Information). According to Equations (2) and (3), the numerically simulated

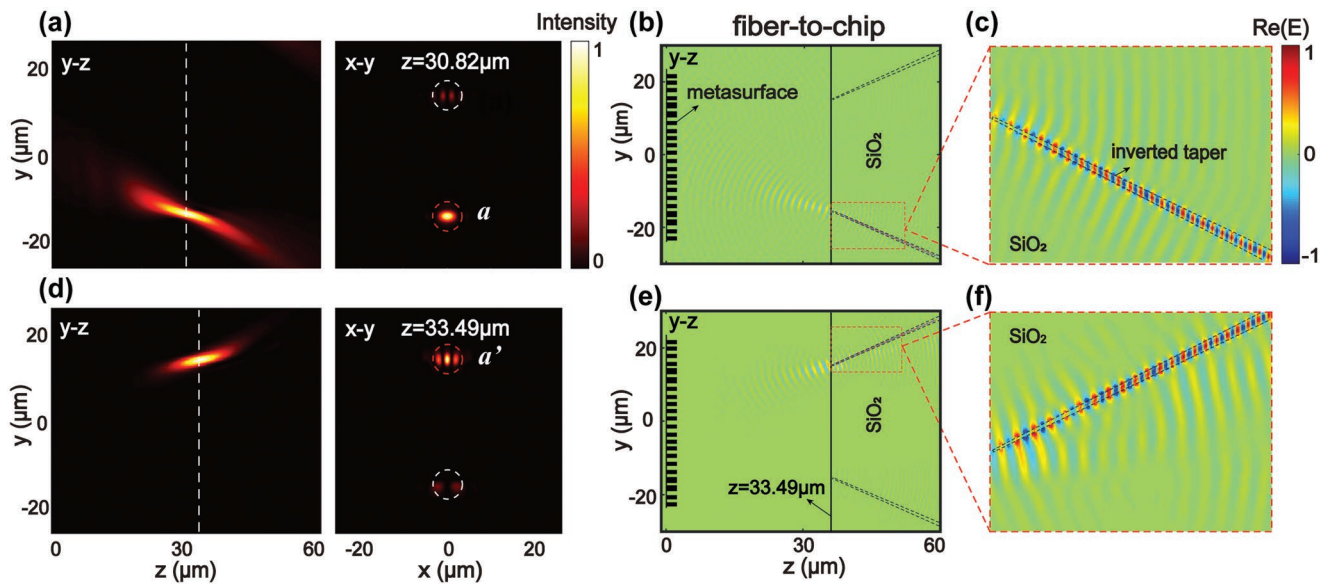


Figure 3. The simulated results of LP_{01} and LP_{11} modes metasurface-based multiplexing coupler. The simulation results of angular spectrum propagation of a) LP_{01} and d) LP_{11} on the y - z and focusing x - y planes via the designed phase profile. FDTD simulation results of b) LP_{01} mode and e) LP_{11} mode impinging onto the metasurfaces, when the cylindrical nanopillars are employed as the metasurface nanostructures. It is noted that the two fiber modes, LP_{01} and LP_{11} , are demultiplexed into the corresponding location and converted into the targeted mode field, propagate well in the wire waveguides as shown in the zoom-in of (c) and (f), respectively.

coupling efficiencies of LP_{01} -to-chip and LP_{11} -to-chip are -8.8 and -12.6 dB, respectively and the simulated crosstalk of both channels is -27.4 and -24.2 dB. Coupling efficiency difference between LP_{01} and LP_{11} modes attributes to the difference mode field profile focused by metasurface in the right half of Figure 3a (one main spot for LP_{01} mode) and d (one main spot with several sidelobes for LP_{11} mode). Such phenomena are also reflected in the following multiplexing couplers. So far, as dual-mode edge coupler, the proposed metasurfaces can simultaneously achieve fiber-to-chip coupling for LP_{01} and LP_{11} for single wavelength of 1550 nm. The spectra performance of this

dual-mode multiplexing coupler is also evaluated from 1500 to 1600 nm (The details can be found in Figure S6, Supporting Information).

It should be noted that the proposed region division scheme is not only suitable for LP_{01} and LP_{11} , but also feasible for higher order modes. As a proof, the investigation of LP_{11b} (Figure 4a) and LP_{21} (Figure 4e) fiber modes is shown in Figure 4. In this case, the phase profile can be divided into four regions with phases, $\phi(x, y; l)$, $\phi(x, y; l) - \pi$, $\phi(x, y; -l)$ and $\phi(x, y; -l)$, as shown in Figure 4b,f. The simulations using angular spectrum method and FDTD method are presented in the right half of

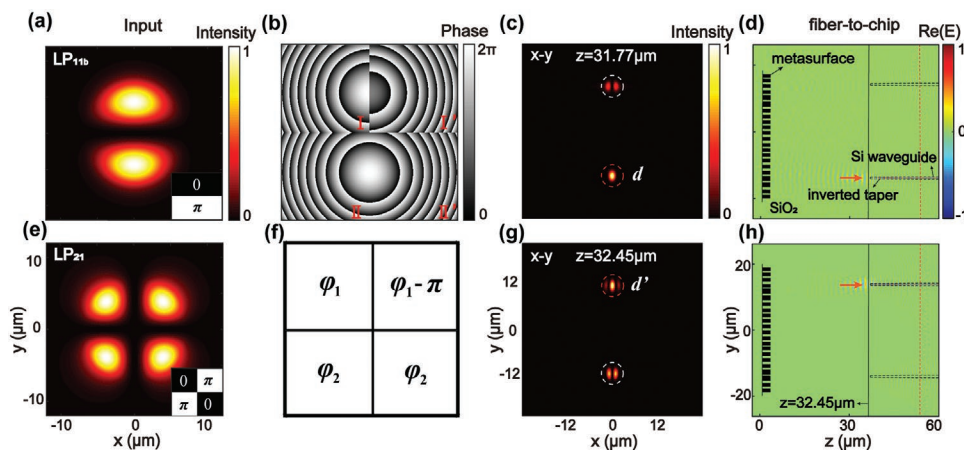


Figure 4. The simulated results of LP_{11b} and LP_{21} mode metasurface-based multiplexing coupler. The amplitude profile of a) LP_{11b} and e) LP_{21} fiber mode, corresponding phase profiles are also shown in the insets of (a) and (e). b) The designed ideal phase profile of four different regions based on f) the region division scheme. The simulation results of angular spectrum propagation of c) LP_{11b} and g) LP_{21} on the focusing x - y plane via the designed ideal phase profile. FDTD simulation results of d) LP_{11b} and h) LP_{21} dual-mode fiber coupled with on-chip waveguides, when the cylindrical nanopillars are employed as the metasurface nanostructures to implement the ideal phase profiles. It is shown that two fiber modes, LP_{11b} and LP_{21} , are demultiplexed into the corresponding location of d and d' , converted into targeted mode fields, propagate well in the wire waveguides, respectively.

Figure 4. For LP_{11} mode, the phase is 0 in the top region and π in the bottom region in the bottom right corner of Figure 4a. After being modulated by the ideal phase profile, we can find that a bright focal spot caused by constructive interference presents at the point d on the y -axis, while a dark focal spot caused by destructive interference appears at the point d' , as shown in Figure 4c. In the contrast, as shown in bottom right corner of Figure 4e, for LP_{21} mode, the phase profile of the left half is same as that of LP_{11} mode while the phase profile of the right half is opposite to that of LP_{11} mode. Therefore, the bright focal spot and dark focal spot exchange the locations for LP_{21} mode, which is reflected in Figure 4c.g. When the ideal profile is implemented using the metasurfaces, as expected, the simulation results indicate that the designed metasurface can achieve selective focusing, demultiplexing of LP_{11} and LP_{21} modes and the coupling of LP_{11} -to-chip and LP_{21} -to-chip, as shown in Figure 4d,h. The simulated coupling efficiencies of two modes are -8.1 and -10.2 dB, respectively, and the simulated crosstalk are -24.4 and -26.2 dB, respectively. Obviously, by adjusting the phase distribution in different regions of the metasurface according to different parities of LP_{11} and LP_{21} modes, the proposed scheme can act as an edge coupler, achieving LP_{11} -to-chip and LP_{21} -to-chip dual-mode coupling simultaneously.

3.2. Triple-Mode Metasurface-Based Multiplexing Coupler

Compared to dual-mode metasurface-based multiplexing coupler, triple-mode case is more challenging, but it can provide high transmission capability. The first triple-mode example is LP_{01} , LP_{11a} , and LP_{11b} . Among them, the phase distribution of LP_{01} is uniform, while the two petals of both LP_{11a} and LP_{11b} have π phase difference, which is reflected in Figure 5a,b. According to the symmetry of the amplitude and phase distributions of those three modes, we divide the metasurfaces into nine blocks as schematically shown in Figure 5a, which are distinguished with $I, II, II', III, III', IV, IV', V$ and V' . The corresponding phase is given as five groups, $\varphi_1 = \phi(x, y; a)$, $\varphi_2 = \phi(x, y; a')$, $\varphi_2' = \phi(x, y; a') - \pi$, $\varphi_3 = \phi(x, y; 0)$, $\varphi_3' = \phi(x, y; 0) - \pi$, $\varphi_4 = \phi(x, y; c)$, $\varphi_4' = \phi(x, y; c) - \pi$, $\varphi_5 = \phi(x, y; c')$, and $\varphi_5' = \phi(x, y; c') - \pi$. The phase profile is shown in Figure 5c.

For group I in Figure 5a, it can separate LP_{01} from other modes and focus it to point a on the y -axis. On the other hand, since the two petals of LP_{11a} and LP_{11b} are out of phase by π , they interfere destructively after being phase-modulated by group I . For group II , π phase delay difference between them can separate LP_{11a} from the triple mode. After the modulation of II and II' , a bright spot produced by LP_{11a} can be found at

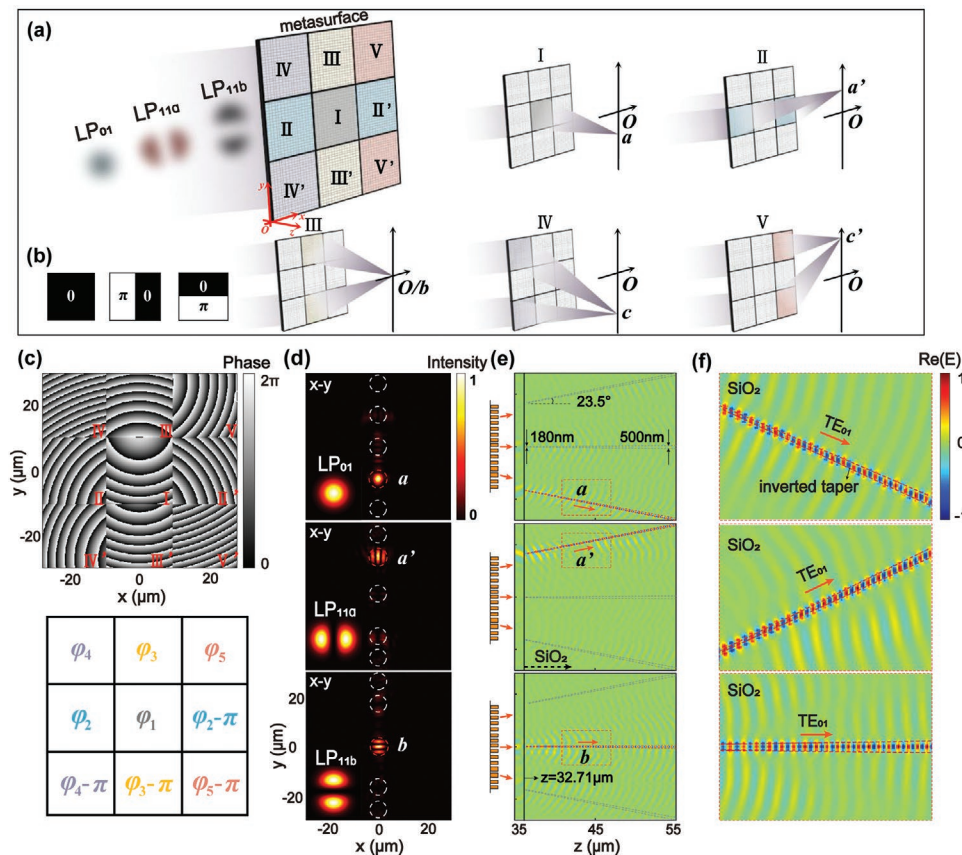


Figure 5. The simulated results of triple-mode, LP_{01} , LP_{11a} , and LP_{11b} , metasurface-based multiplexing coupler. a) The region division scheme for the triple-mode and the location of the corresponding focal spots. b) The phase profile of LP_{01} , LP_{11a} , and LP_{11b} modes. c) The phase profile for the region division scheme. d) Simulation results of angular spectrum propagation of LP_{01} , LP_{11a} , and LP_{11b} on the focusing x - y plane via the designed phase profile. e) FDTD simulation results of LP_{01} (top), LP_{11a} (middle), and LP_{11b} (bottom) triple-mode fiber coupled to on-chip waveguides, when the cylindrical nanopillars are employed as the metasurface nanostructures. As shown in the zoom-in of (f), it is noted that three fiber modes, LP_{01} , LP_{11a} , and LP_{11b} , are demultiplexed into the corresponding location of a , a' , and b , converted into the targeted mode field, propagate well in the wire waveguides, respectively.

point a' on the y -axis. Due to the uniform phase of LP_{01} and the weaker intensity of LP_{11b} for group *II*, they cannot produce a similar bright spot at point a' . Instead, group *III* can achieve the separation of LP_{11b} due to the variation of spatial position. The reasons are similar to that of LP_{11a} case. As seen from Figure 5a, the focal spot locates at the central point b now. Similar to group *III*, group *IV* or *V* can also focus LP_{11a} at the point c or c' , respectively. But in this case, the intensity of the focal spots becomes much weaker compared to the main spot at a , a' and b . Similar phenomena are found for LP_{11b} .

To characterize the function of the designed phase profile in Figure 5c, the normalized intensity distribution at the focal plane of LP_{01} (top), LP_{11a} (middle), and LP_{11b} (bottom) modes are provided in Figure 5d. It is found that the focal spot resulting from LP_{01} occurs at point a , while LP_{11a} for point a' and LP_{11b} for point b . The angular spectrum simulation results indicate that the ideal phase profile can modulate the light and achieve selective focusing and demultiplexing of LP_{01} , LP_{11a} , and LP_{11b} modes. Further, eight cylindrical nanopillars are used as the metasurface nanostructures to sample the phase profile and the FDTD simulations are performed in Figure 5e. The edge of chip is located at $z = 32.71 \mu\text{m}$, where the focal spot is located. The deflection angles of three inverse taper waveguides are 23.5° , 0° , and -23.5° , respectively. It is shown that the couplings of LP_{01} -to-chip, LP_{11a} -to-chip, and LP_{11b} -to-chip are achieved and the converted TE_{01} mode propagates well along

the inverted taper and the following waveguides. The coupling efficiencies are -11.2 , -15.0 , and -12.1 dB, respectively, while the simulated crosstalks of three channels are -170 , -15.1 , and -13.4 dB, respectively. So far, using circular silicon nanopillars with a height of 750 nm , we have achieved triple-mode selective focusing of LP_{01} , LP_{11a} and LP_{11b} , as well as multimode coupling.

Further, another triple-mode, LP_{01} , LP_{11} , and LP_{21} , is investigated in Figure 6. Compared to the previous one, a high-order mode LP_{21} is considered instead of LP_{11} and therefore a different region division scheme should be raised. According to the symmetry of complex amplitude (Figure 6a,b) of considered fiber modes, the focusing of LP_{01} mode requires that the focusing phases are uniform, while the focusing of the LP_{11} mode requires that focusing phases of the left half and right half differ by π . For LP_{21} mode, the focal phase difference of adjacent quadrants is π . Therefore, the ideal phase profile is divided into three group, $\varphi_1 = \phi(x, y; a)$, $\varphi_2 = \phi(x, y; a')$, and $\varphi_3 = \phi(x, y; 0)$. The phase profile and region division scheme are given in Figure 6c.

For group *I*, similar to the previous case in Figure 5, it can focus LP_{01} at the point a of the y -axis, where both LP_{11} and LP_{21} modes have destructive interferences due to the π phase difference in the Figure 6b. For group *II*, it can provide π phase difference between left and right half region, therefore, there are destructive interference for LP_{01} mode and constructive

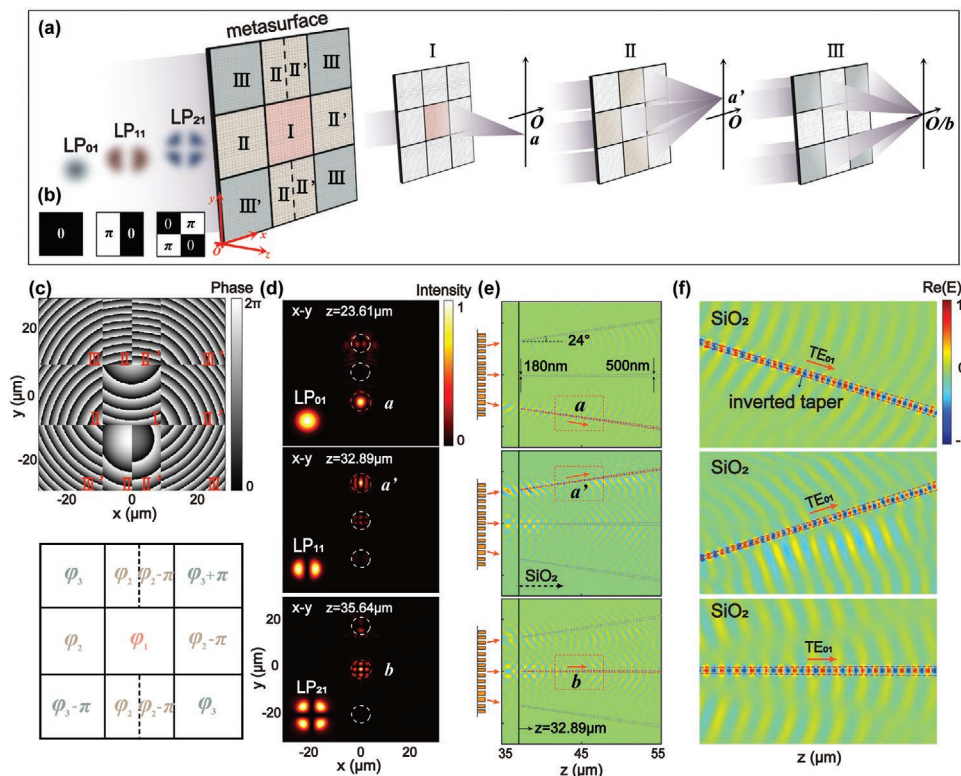


Figure 6. The simulated results of triple-mode, LP_{01} , LP_{11b} , and LP_{21} , metasurface-based multiplexing coupler. a) The region division scheme for the triple-mode and the location of the corresponding focal spots. b) The phase profile for the region division scheme. c) The phase profile for the region division scheme. d) Simulation results of angular spectrum propagation of LP_{01} , LP_{11} , and LP_{21} on the focusing x - y plane via the designed phase profile. e) FDTD simulation results of LP_{01} (top), LP_{11} (middle), and LP_{21} (bottom) triple-mode fiber coupled to on-chip waveguides. As shown in the zoom in (f), three fiber modes, LP_{01} , LP_{11} , and LP_{21} , are demultiplexed into the corresponding location of a , a' , and b , converted into the targeted mode field, propagate well in the wire waveguides, respectively.

interference for LP₁₁ mode at the point *a'*. Differently, LP₂₁ mode shows much weaker intensity at the point *a'* due to its mode field spatial distribution. Hence, the group *II* can focus the LP₁₁ mode to the point *a'*. As for group *III*, it can focus LP₂₁ at the point *b*, since its phase difference satisfies the focusing phase required by LP₂₁.

To demonstrate the above phase design, Figure 6d calculates the field intensity on the focal plane after LP₀₁ (top), LP₁₁ (middle), and LP₂₁ (bottom) fiber modes being phase-modulated by ideal phase profile using angular spectrum method. The simulation results show that the propagation channels of LP₀₁, LP₁₁ and LP₂₁ are *a*, *a'* and *b*, respectively. The predicted weak intensity is also found. Further, the overall process of coupling fiber modes into tapered waveguides are simulated in Figure 6e,f, when the eight cylindrical nanopillars are used as the metasurface nanostructures to implement the ideal phase profile. The angle of inclination of the three SSCs are 24°, 0°, and -24°, and the edge of chip is placed at *z* = 32.89 μm. Through the FDTD simulation, we find that the coupling efficiencies of the three modes (LP₀₁, LP₁₁, LP₂₁) and the chip waveguide are -12.7, -13.3, and -14.6 dB, respectively, while the simulated crosstalk are -21.2 dB, -10.5 dB and -12.8 dB, respectively. As expected, using cylindrical Silicon nanopillars with a height of 750 nm, we have achieved triple-mode selective focusing of LP₀₁, LP₁₁, and LP₂₁, as well as multimode coupling.

3.3. Discussions of Multiplexing Coupler Fabrication

In Sections 3.1 and 3.2, two-mode and triple-mode metasurface-based multiplexing couplers are designed and demonstrated using FDTD simulations. In the proposed multiplexing coupler, to fully exploit numerical aperture (NA) of the metalens (Metasurfaces has focusing ability), a SiO₂ spacer between the fiber end facet and metasurface nanostructures is brought in to allow for beam expansion. Such setting is indeed difficult to be fabricated compared to the example without spacer. Fortunately, great efforts have been made by researchers toward the fabrication of similar meta-devices using electron-beam lithography (EBL), focus ion beam (FIB) milling, photolithography, nanoimprinting, direct laser writing and nanotransfer.^[32,33]

However, nearly all fabricated optical fiber meta-devices at the current stage are composed of lossy metallic materials. Using other dielectric materials like Si in the proposed multiplexing coupler is still a challenge and need further exploration although some simple nanostructures are demonstrated by using EBL technology.^[32] Due to the limitation of the fabrication apparatus, we could not fabrication the multiplexing coupler and experimentally demonstrated it. Therefore, it is necessary and useful for us to propose the possible fabrication scheme. Based on the fabrication method in the literature^[33] and the specific structures of the proposed multiplexing coupler, we propose two possible fabrication schemes, as follows.

1) Connect the fiber facet with the metasurfaces by the bonding method: This fabrication scheme is divided into two steps. The first step is the fabrication of nanostructures on the SiO₂ spacer. Specifically, a 750-nm-thick amorphous Silicon (α -Si) film is deposited on SiO₂ spacer of 250 μm thickness by the inductively coupled plasma-chemical vapor deposition

(ICP-CVD) process. The metasurfaces patterns and the marker are defined in a high-resolution negative resist (for example, hydrogen silsesquioxane, HSQ) by an electron-beam lithography (EBL) system (for example, Vistec EBPG5000 ES). Then, the pattern was transferred into the α -Si film by Inductively Coupled Plasma (ICP) etching using SF₆. The second step is to connect the fiber facet with the fabricated metasurfaces by the bonding method. Be specific, the fabricated metasurfaces with a 250 μm thickness SiO₂ spacer is cut into a suitable cylindrical shape using a femtosecond laser machine. The optical few-mode fiber is firmly fixed using a holder, and the cut metasurfaces is fixed by a motorized platform. With the help of a vision system, the metasurfaces is precisely aligned with the core of the fiber by precise movement of the motorized stage. Finally, the SiO₂ spacer with metasurfaces is glued to the fiber with UV-cured epoxy resin.

2) Splicing an SiO₂ spacer to the fiber and then directly implement metasurfaces nanostructure using EBL: This fabrication scheme is also divided into two steps. The first step is splicing an SiO₂ spacer of 250 μm thickness to a few-mode fiber.^[34] To be more specific, the SiO₂ spacer is realized by splicing a silica coreless fiber of the required diameter to the delivery fiber and then precisely cutting it to the appropriate length of 250 μm. The second step is the nanostructure implementation on the surface of SiO₂ spacer using EBL, which is similar as the first step of the first fabrication scheme. But it should be noted that EBL technology is designed for wafer processing (flat and wide) and is therefore inherently incompatible with the thin and long fiber geometry. Fortunately, the mount way of the fiber in^[35] can be used to overcome this geometry mismatch, which enables us to finish the nanostructure fabrication on the fiber facet as that designed for wafer processing.

For both fabrication schemes, the fabrication tolerance and the misalignment should be investigated due to the tiny geometry of the fiber facet and the metasurface nanostructures, which has a critical influence on the performance of multiplexing couplers. The first one we consider is the influence of Si nanopillar's parameters, including diameter and height of the nanopillar, on the coupling efficiency. We take the two fiber modes for example, LP₀₁ and LP₁₁, to explicitly illustrate the influence of Si nanopillar's parameters on the coupling efficiency (Figure S7, Supporting Information). The second one is the alignment tolerance between multiplexing coupler and the SOI chip waveguide, the details can be found in Figure S8 (Supporting Information). the SOI chip tolerance of ±0.5 μm should be acceptable when the multiplexing coupler is fabricated. The last one is the misalignment of the fiber and metasurfaces due to the inaccuracies in the fabrication, which is shown in Table S1 (Supporting Information).

4. Conclusions

In this paper, we present a metasurface-based fiber-to-chip multiplexing coupler that can simultaneously realize mode conversion and multiplexing coupling between few-mode fibers and on-chip single-mode waveguides. With the ultracompact footprint and low crosstalk, such implementation is beneficial to the integration and miniaturization of the photonics integrated systems.

Compared with single mode coupling that only carries information through fundamental mode, this research explores the application potential of metasurfaces in multimode coupling of FMFs and on-chip waveguides, improving the information transmission capability of fiber-to-chip. Notably, the metasurface-based fiber-to-chip multiplexing coupler is polarization-insensitive, and it can further improve the information transmission capability through polarization multiplexing. This study has broad application prospects in the field of integrated optoelectronics and is expected to break through the bottleneck of traditional technologies and provide new technical ideas for optical interconnection.

However, in the metasurface-based fiber-to-chip multiplexing coupler, there are two points that need to be noticed, which could be our future works. First, the coupling efficiency of the proposed multiplexing coupler is much lower than the traditional fundamental single-model coupler. The reason is that the composite phase profile (including focusing phase profile and the focus shift phase profile) of metasurfaces leads to the destructive interference of light passing different region of metasurfaces. To further reduce coupling loss, the optimization of the phase profile based on a predetermined target is an alternative approach. On the other hand, the reflection from the SOI chip waveguide leads to energy loss and thus designing micro- or nanostructures on the chip waveguide is also helpful for the reduction of coupling loss.

Second, we only carry out theoretical investigation due to the limitation of the experimental condition, which provides an important guidance to the experimental demonstration of the combination of metasurfaces structures and the facet of the fiber. In fact, much efforts has been made by researcher on the fabrication of nanostructures on the fiber facet,^[32,33,36] based on which we propose two possible fabrication schemes. We envisage that both fabrication schemes could be realized once the corresponding equipment is available although it is still a challenging work.

Supporting Information

Supporting Information is available from the Wiley Online Library or from the author.

Acknowledgements

R.C. and Y.-k.C. contributed equally to this work. The authors acknowledge support from the National Key Research and Development Program of China (2022YFA1404304), the National Natural Science Foundation of China (62035016, 61905291, 11874435), and the Guangdong Basic and Applied Basic Research Foundation (2020A1515010626). Fundamental Research Funds for the Central Universities (22qntd3002)

Conflict of Interest

The authors declare no conflict of interest.

Data Availability Statement

The data that support the findings of this study are available from the corresponding author upon reasonable request.

Keywords

few-mode fiber coupling, metasurfaces, mode multiplexing

Received: October 1, 2022

Revised: December 22, 2022

Published online:

- [1] E. Timurdogan, Z. Su, R.-J. Shiuie, M. J. Byrd, C. V. Poulton, K. Jabon, C. DeRose, B. R. Moss, E. S. Hosseini, I. Duzevik, M. Whitson, R. P. Millman, D. A. Atlas, M. R. Watts, in *Optical Fiber Communication Conference 2020*, Optica Publishing Group, San Diego, California, United States **2020**, paper T3H.2.
- [2] H. R. D. Sunak, *IEEE Trans. Instrum. Meas.* **1988**, 37, 557.
- [3] G. Son, S. Han, J. Park, K. Kwon, K. Yu, *Nanophotonics* **2018**, 7, 1845.
- [4] D. Vermeulen, C. V. Poulton, *Proc. IEEE* **2018**, 106, 2270.
- [5] Y. Wang, X. Wang, J. Flueckiger, H. Yun, W. Shi, R. Bojko, N. A. F. Jaeger, L. Chrostowski, *Opt. Express* **2014**, 22, 20652.
- [6] D. Benedikovic, C. Alonso-Ramos, P. Cheben, J. H. Schmid, S. Wang, D. X. Xu, J. Lapointe, S. Janz, R. Halir, A. Ortega-Moñux, J. G. Wangüemert-Pérez, I. Molina-Fernández, J. M. Fédéli, L. Vivien, M. Dado, *Opt. Lett.* **2015**, 40, 4190.
- [7] M. Dai, L. Ma, Y. Xu, M. Lu, X. Liu, Y. Chen, *Opt. Express* **2015**, 23, 1691.
- [8] D. Taillaert, F. Van Laere, M. Ayre, W. Bogaerts, D. Van Thourhout, P. Bienstman, R. Baets, *Jpn. J. Appl. Phys.* **2006**, 45, 6071.
- [9] M. Papes, P. Cheben, D. Benedikovic, J. H. Schmid, J. Pond, R. Halir, A. Ortega-Moñux, G. Wangüemert-Pérez, W. N. Ye, D. X. Xu, S. Janz, M. Dado, V. Vašinek, *Opt. Express* **2016**, 24, 5026.
- [10] L. Jia, C. Li, T. Y. Liow, G. Q. Lo, *J. Lightwave Technol.* **2018**, 36, 239.
- [11] Y. Liu, W. Sun, H. Xie, N. Zhang, K. Xu, Y. Yao, S. Xiao, Q. Song, *IEEE J. Sel. Top. Quantum Electron.* **2019**, 25, 4700106.
- [12] A. Khilo, M. A. Popović, A. Araghchini, F. X. Kärtner, *Opt. Express* **2010**, 18, 15790.
- [13] H. Park, S. Kim, J. Park, J. Joo, G. Kim, *Opt. Express* **2013**, 21, 29313.
- [14] P. Cheben, J. H. Schmid, S. Wang, D.-X. Xu, M. Vachon, S. Janz, J. Lapointe, Y. Painchaud, M.-J. Picard, *Opt. Express* **2015**, 23, 22553.
- [15] Y. Lai, Y. Yu, S. Fu, J. Xu, P. P. Shum, X. Zhang, *Opt. Lett.* **2018**, 43, 3172.
- [16] Y. Lai, Y. Yu, S. Fu, J. Xu, P. P. Shum, X. Zhang, *Opt. Lett.* **2017**, 42, 3702.
- [17] Z. Li, Y. Lai, Y. Yu, X. Zhang, *IEEE Photonics Technol. Lett.* **2020**, 32, 371.
- [18] W. Shen, J. Du, J. Xiong, L. Ma, Z. He, *Opt. Express* **2020**, 28, 33254.
- [19] Y. Wu, K. S. Chiang, *Opt. Lett.* **2017**, 42, 407.
- [20] J. L. Dong, K. S. Chiang, W. Jin, *Opt. Lett.* **2015**, 40, 3125.
- [21] N. Yu, A. Genevet, M. A. Kats, F. Aieta, J.-P. Tetienne, F. Capasso, Z. Gaburro, *Science* **2011**, 334, 333.
- [22] S. L. Sun, K. Y. Yang, C. M. Wang, T. K. Juan, W. T. Chen, C. Y. Liao, Q. He, S. Y. Xiao, W. T. Kung, G. Y. Guo, L. Zhou, D. P. Tsai, *Nano Lett.* **2012**, 12, 6223.
- [23] A. Arbabi, Y. Horie, A. J. Ball, M. Bagheri, A. Faraon, *Nat. Commun.* **2015**, 6, 7069.
- [24] Z. B. Fan, Z. K. Shao, M. Y. Xie, X. N. Pang, W. S. Ruan, F. L. Zhao, Y. J. Chen, S. Y. Yu, J. W. Dong, *Phys. Rev. Appl.* **2018**, 10, 014005.
- [25] Z. P. Zhuang, R. Chen, Z. B. Fan, X. N. Pang, J. W. Dong, *Nanophotonics* **2019**, 8, 1279.
- [26] F. Ding, Z. Wang, S. He, V. M. Shalaev, A. V. Kildishev, *ACS Nano* **2015**, 9, 4111.
- [27] M. Q. Mehmood, S. Mei, S. Hussain, K. Huang, S. Y. Siew, L. Zhang, T. Zhang, X. Ling, H. Liu, J. Teng, A. Danner, S. Zhang, C. W. Qiu, *Adv. Mater.* **2016**, 28, 2533.

- [28] H. Chen, Z. Chen, Q. Li, H. Lv, Q. Yu, X. Yi, *J. Mod. Opt.* **2015**, *62*, 638.
- [29] S. Kruk, F. Ferreira, N. M. Suibhne, C. Tsekrekos, I. Kravchenko, A. Ellis, D. Neshev, S. Turitsyn, Y. Kivshar, *Laser Photonics Rev.* **2018**, *12*, 1800031.
- [30] E. Nazemosadat, M. Mazur, S. Kruk, I. Kravchenko, J. Carpenter, J. Schröder, P. A. Andrekson, M. Karlsson, Y. Kivshar, *Adv. Opt. Mater.* **2019**, *7*, 1801679.
- [31] V. Liu, S. Fan, *Comput. Phys. Commun.* **2012**, *183*, 2233.
- [32] Y. Meng, Y. Chen, L. Lu, Y. Ding, A. Cusano, J. A. Fan, Q. Hu, K. Wang, Z. Xie, Z. Liu, Y. Yang, Q. Liu, M. Gong, Q. Xiao, S. Sun, M. Zhang, X. Yuan, X. Ni, *Light: Sci. Appl.* **2021**, *10*, 235.
- [33] Q. Zhao, W. Yuan, J. Qu, Z. Cheng, G.-D. Peng, C. Yu, *Nanomaterials* **2022**, *12*, 793.
- [34] M. Zeisberger, H. Schneidewind, U. Hübner, T. Wieduwilt, M. Plidschun, M. A. Schmidt, *Adv. Photonics Res.* **2021**, *2*, 2100100.
- [35] N. Wang, M. Zeisberger, U. Hübner, M. A. Schmidt, *Opt. Mater. Express* **2018**, *8*, 2246.
- [36] N. Yu, F. Capasso, *J. Lightwave Technol.* **2015**, *33*, 2344.